



Cascade of the delocalization transition in a non-Hermitian interpolating Aubry-André-Fibonacci chain

Liang-Jun Zhai ^{1,2}, Guang-Yao Huang,^{3,*} and Shuai Yin ^{4,†}

¹*The School of Mathematics and Physics, Jiangsu University of Technology, Changzhou 213001, China*

²*Department of Physics, Nanjing University, Nanjing 210093, China*

³*Institute for Quantum Information & State Key Laboratory of High Performance Computing, College of Computer, National University of Defense Technology, Changsha 410073, China*

⁴*School of Physics, Sun Yat-Sen University, Guangzhou 510275, China*



(Received 25 April 2021; revised 18 June 2021; accepted 24 June 2021; published 1 July 2021)

In this paper, the interplay of the non-Hermiticity and the cascade of delocalization transition in a quasiperiodic chain are studied. The study is applied in the non-Hermitian interpolating Aubry-André-Fibonacci (IAAF) model, which combines the non-Hermitian Aubry-André (AA) model and the non-Hermitian Fibonacci model through a varying parameter, and the non-Hermiticity in this model is introduced by nonreciprocal hopping. In the non-Hermitian AA limit, the system undergoes a delocalization transition by tuning the potential strength. At the critical point, the spatial distribution of the critical state shows a self-similar structure with the relative distance between the peaks being the Fibonacci sequence, and the finite-size scaling of the inverse participation ratios (IPRs) of the critical ground state with lattice size L shows that $\text{IPR}_g \propto L^{-0.1189}$. In the non-Hermitian Fibonacci limit, we find that the system is always in the extended phase. Along the continuous deformation from the non-Hermitian AA model into the non-Hermitian Fibonacci model in the IAAF model, the cascade of the delocalization transition is found, but only a few plateaux appear. Moreover, the self-similar structure of spatial distribution for the critical modes along the cascade transition is also found. In addition, we find that the delocalization transition and the real-complex transition for the excited states happen at almost the same parameter. Our results show that the non-Hermiticity provides an additional knob to control the cascade of the delocalization transition besides the on-site potential.

DOI: [10.1103/PhysRevB.104.014202](https://doi.org/10.1103/PhysRevB.104.014202)

I. INTRODUCTION

In a quasiperiodic system, unlike the periodic system, the translational invariance is broken by the incommensurate period, but unlike the disordered system, the long-range correlation still persists. These special features make the quasiperiodic system not only inherit the physics of both periodic and disordered systems, such as Anderson localization [1–4], but also exhibit lots of novel phenomena, such as the fractal eigenmodes [5–8].

Many theoretical quasiperiodic models [1–6], including the bichromatic lattices [7], electronic materials in orthogonal magnetic field [9], have been proposed to study the delocalization transition and the critical behavior. In particular, many one-dimensional models have been intensively studied due to its simplicity and experimental realization [10–25]. Among these models, the Aubry-André model (AA) [1,2,12–18] and the Fibonacci model [6,19–24] are two of the most celebrated examples. For the AA model, the quasiperiodicity enters in the form of an on-site cosine modulation incommensurate with the underlying periodic lattice spacing, and the delocalization transition occurs at a critical value of the quasiperiodic

potential [1]. For the Fibonacci model, the potential is a binary chain, and it has a modulation with two discrete values that appear interchangeably according to the Fibonacci sequence [6,19–23]. Theoretical and experimental studies have shown that the Fibonacci model always has critical wave functions for any value of the quasiperiodic potential [6,21–25]. Moreover, recently it was shown that many exotic properties appear in the interpolating Aubry-André-Fibonacci (IAAF) model, which combines the AA model and the Fibonacci model [11,25,26]. Based on the IAAF model, the AA model and the Fibonacci model share the same topological properties and belong to the same topological class [26]. Despite these two limits, there is a wide range of parameter space unexplored in the IAAF model. With both theoretical and experimental efforts, Ref. [25] finds that a cascade of delocalization transition occurs when the interpolating parameter runs from the limit of AA model to the limit of the Fibonacci model.

On the other hand, the delocalization transition is also found in the non-Hermitian disordered and quasiperiodic systems [27–45]. Due to the releasing of Hermiticity constrain, non-Hermitian systems exhibit much richer phenomena than their Hermitian counterparts [46–51], such as the topological non-Hermitian skin effect under open boundary condition (OBC) [52–64], exceptional points [65–69], etc. Many interesting critical behaviors were found in the non-Hermitian systems [70–73], and the fundamental concepts in the usual

*guangyaohuang@quanta.org.cn

†yinsh6@mail.sysu.edu.cn

critical systems, such as, the band gaps and locality, have been challenged [72,73]. Moreover, effects induced by the non-Hermiticity in the delocalization transition have been studied in different contexts [27–40].

Here we investigate the effect of non-Hermiticity in the cascade of the delocalization transition in the IAAF model. By introducing the nonreciprocal hopping term, we construct a non-Hermitian IAAF model. In the non-Hermitian AA limit, the system shows a delocalization transition by tuning the strength of the quasiperiodic potential, while in the non-Hermitian Fibonacci model limit, we find this model is always in the extended phase. Along the continuous deformation from the non-Hermitian AA limit into the non-Hermitian Fibonacci limit, the cascade of the inverse participation ratios (IPRs) is found, similar to its Hermitian counterpart [25]. However, we find that for the non-Hermitian IAAF model, there are only a few plateaux. This is quite different from the Hermitian case [25]. Moreover, the critical properties of the delocalization transition are also studied. In particular, the coincidence between the delocalization transition and the real-complex transition is verified. Our results demonstrate that the non-Hermiticity provides an additional knob to control the cascade of the delocalization transition.

The remainder of the paper is organized as follows. In Sec. II, the non-Hermitian IAAF model is presented. In Sec. III, the delocalization transition and critical behavior of the non-Hermitian AA limit and the non-Hermitian Fibonacci limit are studied. Then, the cascade of delocalization transition along the continuous deformation from the non-Hermitian AA model into the non-Hermitian Fibonacci model is explored in Sec. IV. The experimental feasibility is discussed in Sec. V. A summary is given in Sec. VI. In the Appendix, we show other indicators of the cascade of the delocalization transition.

II. THE NON-HERMITIAN IAAF MODEL

In this paper, the non-Hermiticity is induced by nonreciprocal hopping. The non-Hermitian IAAF model then reads

$$H = \sum_{j=1}^L (te^g c_{j+1}^+ c_j + te^{-g} c_j^+ c_{j+1}) + \lambda V_j(\beta) c_j^+ c_j, \quad (1)$$

where c_j^+ (c_j) are creation (annihilation) operators at site j , λ measures the strength of the on-site potential, and L is the lattice size; t and g label the nonreciprocal hopping between nearest-neighbor sites. In the following, we assume $t = 1$ as the unit of energy.

The on-site potential $V_j(\beta)$ is written as [25]

$$V_j(\beta) = -\frac{\tanh\{\beta[\cos(2\pi\alpha j + \phi) - \cos(\pi\alpha)]\}}{\tanh \beta}, \quad (2)$$

where ϕ is a random phase, and β is a tunable parameter, and α is an irrational spatial modulation frequency. For the infinity system, α is usually chosen to be the inverse golden ratio $(\sqrt{5} - 1)/2$, which can be approached by $\alpha = \lim_{n \rightarrow \infty} F_n/F_{n+1}$ with F_n being the n th Fibonacci number. For the finite system with the periodic boundary condition (PBC), the potential must be periodic and α has to be approximated by a rational number F_n/F_{n+1} with site number $L = F_{n+1}$.

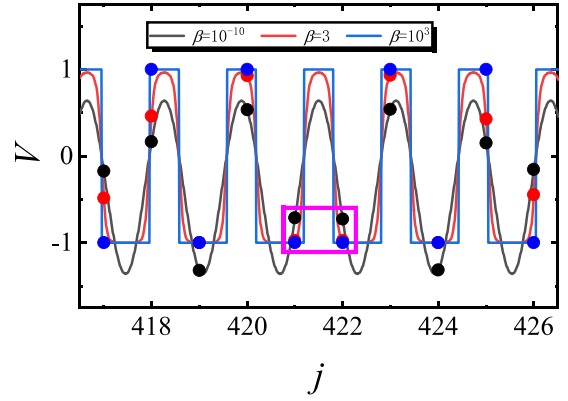


FIG. 1. Evolution of the spatial on-site potential for several values of β . The discrete values of $V_j(\beta)$ are sampled. Here we set $\phi = 0$.

For very small β , like $\beta = 10^{-10}$, the on-site potential $V_j(\beta)$ reduces to $V_j = \cos(2\pi\alpha j + \phi) - \cos(\pi\alpha)$, which is the AA modulation with a constant energy shift. With the increase of β , the continuous function of $V_j(\beta)$ becomes steeper as shown in Fig. 1, and the range of possible values of V_j shrinks. For very large β , like $\beta = 10^3$, $V_j(\beta)$ becomes a step potential switching between ± 1 according to the Fibonacci sequence. As a result, the model (1) can be continuously changed from the non-Hermitian AA model to the non-Hermitian Fibonacci model by tuning β .

III. THE DELOCALIZATION TRANSITION AND CRITICAL BEHAVIOR IN THE NON-HERMITIAN AA AND THE NON-HERMITIAN FIBONACCI LIMIT

A. The non-Hermitian AA limit

For the Hermitian AA model, all states are extended for $\lambda/t < 2$, and they are localized for $\lambda/t > 2$, and at $\lambda/t = 2$ all states are critical [1]. It was shown that the nonreciprocal hopping changes the critical point between the extended phases and the localization phase to be [34]

$$\lambda_c = 2te^g. \quad (3)$$

The phase diagram ($g > 0$) of the non-Hermitian AA model is given in Fig. 2(a). When $\lambda < 2te^g$, the non-Hermitian AA model is in the extended phase. In this phase, the system has an edge state under the OBC due to the non-Hermitian skin effect [52]. When $\lambda > 2te^g$, the non-Hermitian AA model is in the localized phase, and the localized state has an asymmetrical exponential decay under both the PBC and the OBC, which demonstrates different localization lengths on different sides from the localization center. Moreover, it has been demonstrated that $\lambda_c = 2te^g$ is also the boundary between the topologically trivial and the nontrivial phases [34], i.e., the localization phase is also the topological trivial phase with zero winding number, and the extended phase corresponds to the topological nontrivial phase with the winding number being 1 for $g > 0$. Due to the bulk-bulk correspondence [34], the extended phase of $g > 0$ should have a right-skin edge state under OBC.

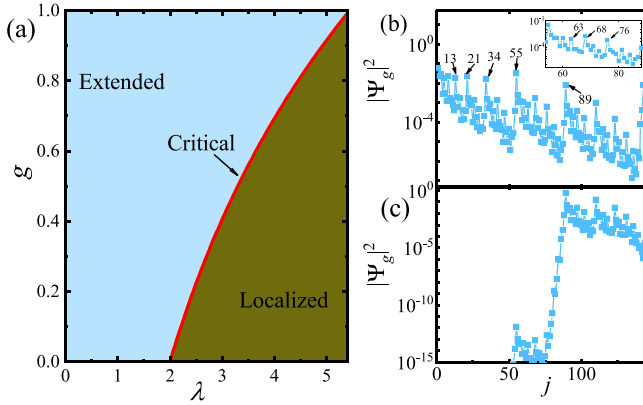


FIG. 2. (a) Phase diagram of the non-Hermitian AA model. The blue region is the extended phase, and the yellow region is the localized phase, and the red curve separating these two regions is the critical line. Typical spatial distributions of the $|\Psi_g(j)|^2$ in the critical phase under (b) PBC and (c) OBC. In (b) and (c), we set $g = 0.5$, $\phi = 0$, $L = 144$, and $\beta = 10^{-10}$ in the numerical calculation. Some locations of the peaks of $|\Psi_g(j)|^2$ are labeled. The inset in (b) shows the spatial distribution of $|\Psi_g(j)|^2$ between $j = 55$ and 88 .

At $\lambda_c = 2te^g$, the states of the system are all critical. A significant feature of the critical state is the self-similar behavior in the spatial distribution. Here we use the right ground state Ψ_g in the critical phase with $L = 144$ and $\phi = 0$ as an example to illustrate the self-similar structure. It should be noted that the eigenstates are arranged in a descending order of the real parts of the eigenenergies. Accordingly, the ground state corresponds to the eigenstate with the lowest real part of eigenenergy. As shown in Fig. 2(b), the typical spatial distribution of the critical ground state under PBC is plotted. It is found that the peaks of the spatial distribution always satisfy the Fibonacci sequence, i.e., the locations of peak values are $1, 2, 3, \dots, 55, 89, 144$ as labeled in Fig. 2(b). Moreover, the relative distance between secondary peaks located between the primary peaks also satisfy the Fibonacci sequence; for example, the relative distance between the secondary peaks ranging from 55 to 89 also satisfies the Fibonacci sequence as shown in the inset of Fig. 2(b). This self-similar structure is also verified for other lattice sizes and different ϕ . In Fig. 2(c), the spatial distribution of the critical state under the OBC is plotted. One finds that the wave function is localized near the right side, but different from the skin effect, the wave function is not localized on the boundary.

To further study the behavior of the critical mode, we calculate the IPR of the right eigenstate Ψ_n of the Hamiltonian [25,35],

$$\text{IPR}_n = \frac{\sum_{j=1}^L |\Psi_n(j)|^4}{\sum_{j=1}^L |\Psi_n(j)|^2}, \quad (4)$$

where n labels the n th eigenstate of system according to the real part of the eigenvalues. IPR_n is usually used to detect the delocalization transition in both the Hermitian and the non-Hermitian systems [34,35,74,75]. For the extended state, IPR_n scales with L as $\text{IPR}_n \propto L^{-1}$, while for the localized mode IPR_n scales as $\text{IPR}_n \propto L^0$ [25,74].

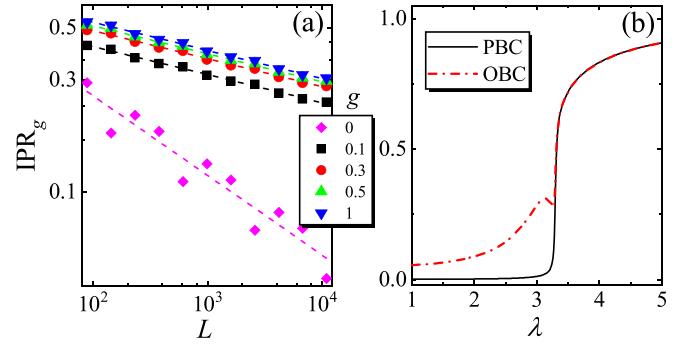


FIG. 3. (a) Finite-size scaling of IPR_g of the critical ground state versus different lattice size L under PBC for various g . The dashed lines are fitting lines. (b) IPR_g versus λ for $g = 0.5$ under PBC and OBC. Here we use $L = 610$ and $\beta = 10^{-10}$, and thus the system is in the AA model limit.

Moreover, it was shown that the IPR of the critical mode also satisfies a power law with respect to L [74,75]. As shown in Fig. 3(a), the L dependence of IPR of the critical ground state (IPR_g) for $\phi = 0$ and different g are plotted. It is found that curves of IPR_g versus L are parallel straight lines in the log-log scale, which demonstrates that IPR_g scales as $\text{IPR}_g \propto L^\nu$ for any $g \neq 0$. By a linear fitting, the average ν is found to be $\nu = -0.1189$. Moreover, the IPR_g versus L and the fitted line for $g = 0$ is also plotted in Fig. 3(a) as a comparison, and the fitted result shows $\nu = -0.2539$, which demonstrates that the non-Hermitian and Hermitian AA models belong to different universal classes [76,77].

In addition, the averaged IPR_g over 500 choices of ϕ as a function of λ under the PBC and OBC is plotted in Fig. 3(b). In the regime of localized phase, the IPR_g under both the PBC and the OBC is almost the same. In contrast, in the regime of extended phase, the IPR_g under OBC is larger than that under PBC. This is because the boundary localization is induced by the nonreciprocal hopping with the OBC [34,52]. More interestingly, we find that under OBC a local minimum of IPR_g develops at $\lambda \approx 3.27$, which is close to the theoretical critical point with $2e^{0.5} \approx 3.29$. A possible reason for the appearance of this local minimum is that in the hopping-dominated extended phase, although the localization induced by the quasiperiodic potential is weakened, the boundary localization induced by the asymmetric hopping is enhanced. When the influence of the boundary localization is stronger than that of the hopping-induced extension, IPR_g increases as λ decreases. This is just the case near the critical point. In contrast, when the influence of the boundary localization is weaker than that of the hopping-induced extension, IPR_g decreases as λ decreases. This is the case for much smaller λ .

B. The non-Hermitian Fibonacci limit

At $g = 0$, it is well known that all the eigenstates are always critical at any $\lambda/t > 0$, and the spatial distribution of the critical mode has a self-similar structure [22,25]. However, for the non-Hermitian Fibonacci model, the eigenstates are in the extended phase [24], and the self-similar structure is destroyed by the non-Hermiticity.

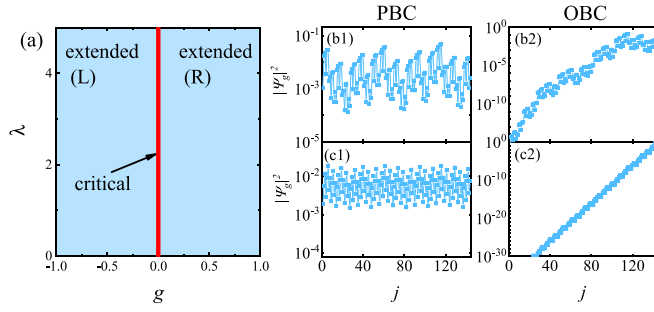


FIG. 4. (a) The phase diagram of the non-Hermitian Fibonacci model. (L) and (R) represent the left-skin and right-skin extended phase. Typical spatial distributions for the eigenstates of the non-Hermitian Fibonacci model under PBC and OBC are shown in (b1), (b2), (c1), and (c2). Here we use $L = 144$, $\lambda = 5$, $\beta = 10^{10}$, $\phi = 0$, and $g = 0.1$ for (b1) and (b2) and $g = 2$ for (c1) and (c2).

The phase diagram of the non-Hermitian Fibonacci model is sketched in Fig. 4(a). The typical spatial distributions of the eigenstates with different g under PBC and OBC are plotted in Figs. 4(b1), 4(b2), 4(c1), and 4(c2). Under the PBC, the spatial distribution of the ground state has a self-similar structure for small g , but it tilts owing to the effect of the nonreciprocal hopping, as shown in Fig. 4(b1) for $g = 0.1$. In contrast, for larger g , the self-similar structure fades away, as plotted in Fig. 4(c1) for $g = 2$. In addition, the difference of the distribution on different sites becomes smaller. Under OBC, as a result of the skin effect [34], the edge states appear on the right boundary for $g > 0$ as shown in Figs. 4(b2) and 4(c2). For $g < 0$, similar behaviors of spatial distribution can also be found, but the edge state should be localized on the left boundary. Apparently, the non-Hermitian Fibonacci model should undergo a transition between the left-skin extended phase and the right-skin extended phase, when g varies from negative to positive.

In Fig. 5(a), the behavior of IPR_g versus L is studied for different g . It is found that IPR_g scales as $\text{IPR}_g \propto L^\nu$ for different g . A power-law fitting shows that the averaged ν is -0.9932 , close to -1 , which means that the non-Hermitian

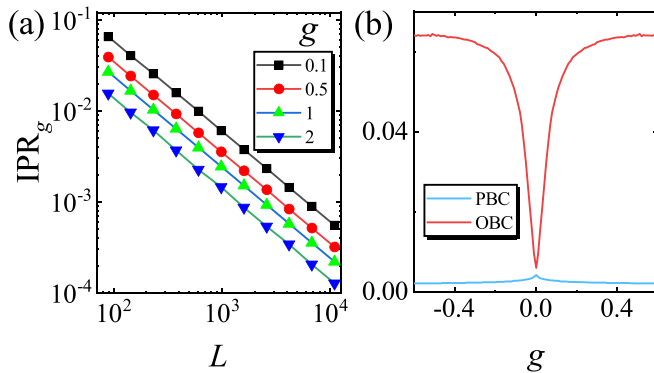


FIG. 5. (a) IPR_g versus L for different g and $\beta = 10^{10}$ (close to the non-Hermitian Fibonacci limit). (b) IPR_g versus g under PBC and OBC for $\beta = 10^{10}$; $\lambda = 5$ is used in the numerical calculation, and the lattice size is $L = 610$ in (b). Both of the results in (a) and (b) are averaged for 500 choices of ϕ .

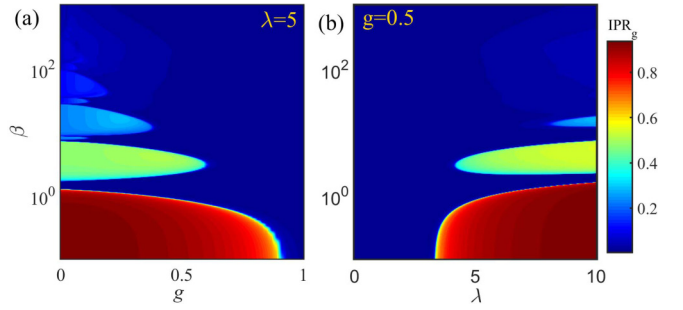


FIG. 6. (a) IPR_g under PBC as a function of β and g for $\lambda = 5$ and (b) IPR_g under PBC as a function of β and λ for $g = 0.5$. The system size is chosen as $L = 610$. IPR_g is averaged for 100 choices of ϕ .

Fibonacci model is in the extended phase for any $g \neq 0$. The IPR_g under PBC and OBC as a function of g are also plotted in Fig. 5(b), and the minimum of IPR_g under OBC and the peak of IPR_g under PBC are found at $g = 0$, indicating that the Hermitian Fibonacci model is in the critical phase separating the left-skin and right-skin phases.

IV. CASCADE OF THE IPR ALONG THE TRANSITION FROM THE AA MODEL TO THE FIBONACCI MODEL

Here we study the delocalization in the non-Hermitian IAAF model (1).

A. Ground state

First, we show the cascade of IPR in the ground state. In Fig. 6(a), the IPR_g versus β and g for $\lambda = 5$ is plotted. For small g , IPR_g shows a cascade behavior, in which the lobes of localization regions with large IPR_g are separated by the delocalization transitions with the minima of IPR_g . This phenomenon is similar to the Hermitian case [25]. But, for large β , the localized regions shrink, since the Fibonacci limit of the non-Hermitian IAAF is always in the extended phase. This is different from the Hermitian case [25], in which the extended region shrinks as β increases, since therein the extended region is suppressed by the critical phase hosted by the Fibonacci limit. For large g , one finds that the number of plateaux of IPR_g becomes small. Such behavior of IPR_g demonstrates that the nonreciprocal hopping tends to destroy the localization. Then, the IPR_g under PBC as a function of β and λ at $g = 0.5$ is plotted in Fig. 6(b). The cascade behavior also manifests itself in this case. For larger λ , the number of plateaux increases.

From Figs. 6(a) and 6(b), one finds that the cascade behavior in the non-Hermitian IAAF model can be tuned by g . For small g and large λ , the behavior is similar to the the Hermitian case [25] when β is small. But for large β , the cascade behavior disappears. This is quite different from the Hermitian case, in which the cascade will continue to $\beta \rightarrow \infty$ as long as the resolution for the IPR_g is high enough.

The mechanism of the cascade behavior is similar to the Hermitian case [25]. In the AA model limit, the ground eigenstates of the strong localized mode are always localized at a single site, and the value of IPR_g is almost 1. With the

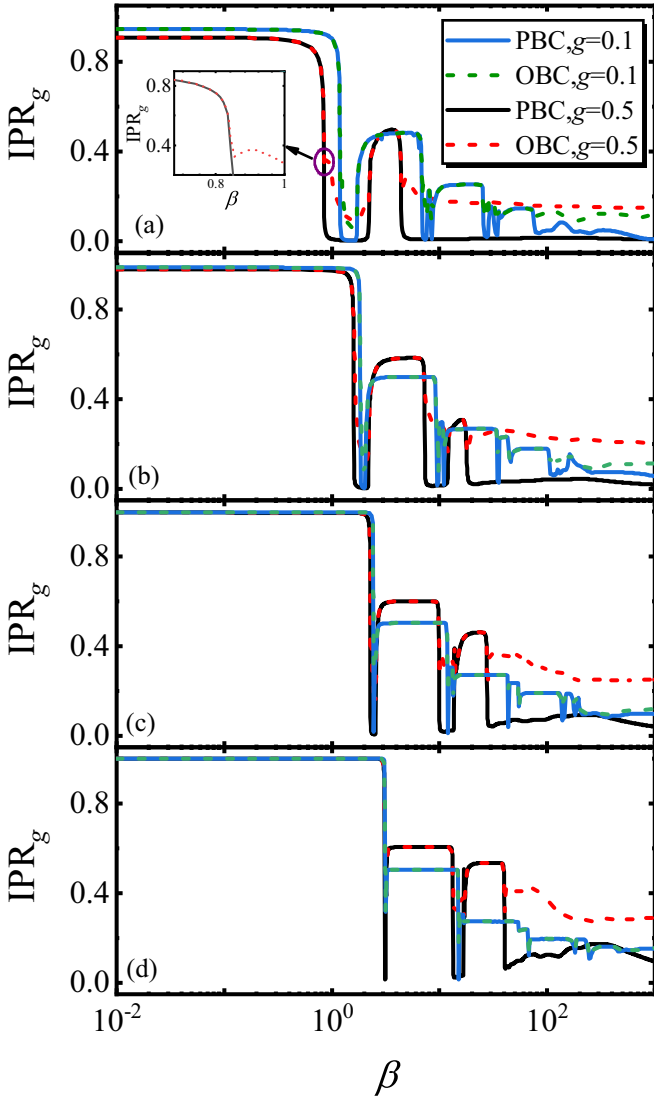


FIG. 7. IPR_g as a function of β for different λ and g under PBC and OBC. Here we use $\lambda = 5$ in (a), $\lambda = 10$ in (b), $\lambda = 20$ in (c), and $\lambda = 50$ in (d), and $L = 610$. The result is averaged for 500 choices of ϕ . The inset in (a) shows the location of critical phase between the first plateau and the transition region.

increase of β , the potential of the two-site pair, two neighbor sites having almost the same potential goes down toward the minimum of the potential, e.g., the sites 421 and 422 labeled in Fig. 1. Thus, the energy of the two-site localized state decreases and the two-site localized state becomes the new ground state [25]. In the transition region between the single site localization and the two-site localization, the system is in the extended phase. The IPR_g decreases suddenly once the system enters into the transition region from the localized phase and then increases when the two-site localized states become the ground states. Similarly, with the further increase of β , the potential values of higher-site groups, like the four-site groups, eight-site groups, and so on, will become the lowest potential, and the corresponding localized states turn into the ground state successively. Therefore, the similar structure of IPR_g appears again. As a result, the IPR_g shows the cascade behavior with the increase of β .

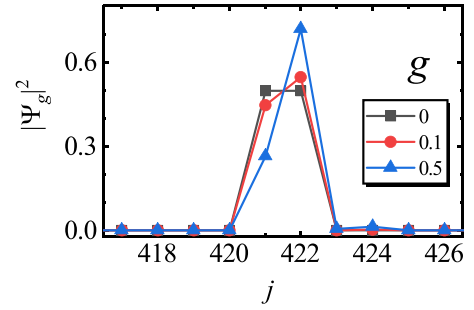


FIG. 8. Typical spatial distribution of the two-site localization state with $g = 0$, $g = 0.1$, and $g = 0.5$. Here we use $\lambda = 10$, $\beta = 5$, $L = 610$, and $\phi = 0$.

However, different from the Hermitian case, there is only a few plateaux in the non-Hermitian IAAF model. To explore the reason, we find that for the Hermitian IAAF model, by increasing $\beta \rightarrow \infty$, the IPR will display a series of plateaux corresponding to the two-site localization mode, four-site localization mode, eight-site localization mode, and so on. Therefore, the localized modes gradually extend to critical in the Fibonacci limit, where the eigenstates are self-similar [25]. But the non-Hermitian Fibonacci model is in the extended states. The self-similarity is truncated for some energy levels. This makes the number of the plateaux limited to a small value.

To further explore the cascade of delocalization transitions, the IPR_g versus β under PBC and OBC for some fixed values of λ and g is shown in Fig. 7. For small β , the values of the IPR_g under the PBC and the OBC coincide in the localized plateaux. However, in the delocalization transition regions, the IPR_g under OBC is larger than that under PBC. The reason is that for the OBC, the IPR_g always has a larger finite value as shown in Figs. 3 and 5, as a result of the skin effect. In addition, Fig. 7(a) shows that, for $\lambda = 5$, the value of the IPR_g in the first plateau decreases as g increases. The reason is that

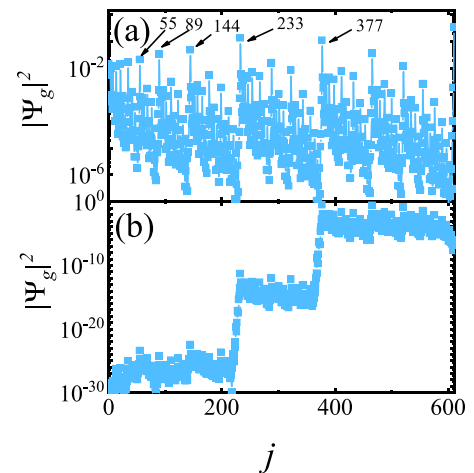


FIG. 9. Typical spatial distribution of critical ground along the transition from the AA model to the Fibonacci model under PBC (a) and OBC (b). Here we use $\lambda = 5$, $\beta = 0.85$, $L = 610$, $g = 0.5$, and $\phi = 0$. These parameters correspond to the minimum of IPR_g under OBC as shown in the inset in Fig. 7(a).

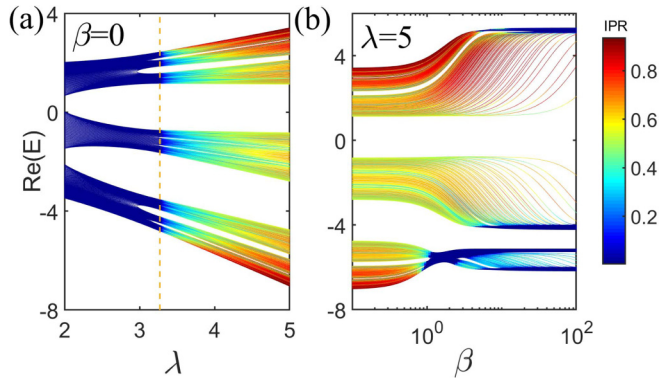


FIG. 10. (a) IPR of all eigenstates of Eq. (1) as a function of the real part of the eigenenergy and λ in the non-Hermitian AA limit. The dashed line is $\lambda_c = 2e^g$. (b) IPR of all eigenstates of Eq. (1) as a function of the real part of the eigenenergy and β ; $g = 0.5$ is used in (a); $g = 0.5$ and $\lambda = 5$ are used in (b). The lattice size is $L = 610$, and the PBC is assumed.

for large g the hopping is enhanced while the localization is suppressed. For the same reason, the transition region between two plateaux is much broader for larger g . With the increase of λ , one finds that first plateaux of $g = 0.5$ and $g = 0.1$ overlap with each other and the transition region shrinks, as shown in Figs. 7(b), 7(c), and 7(d).

Another interesting feature of the cascade behavior is that the IPR_g in the subsequent plateaux (if it exists) becomes larger for larger g for any λ , in contrast to the case for the first plateau. As noted above, these plateaux correspond to the ground state with the two or higher-site localized modes. For the Hermitian case, the eigenstate is equally distributed in these sites [25]. However, for the non-Hermitian Hamiltonian, the distribution weight is different for different sites [34]. As shown in Fig. 8, the spatial distribution of ground states of the two-site localized modes for $g = 0, 0.1$, and 0.5 are plotted. Here we use $\lambda = 10$, $\phi = 0$, and $\beta = 5$, and the sites 421 and 422 are the two-site pairs with the lowest potential. It is clear the eigenstate is equally distributed on these two sites for $g = 0$. However, with the growth of g , the distribution weight on the right site 422 becomes greater than that of the left site 421 owing to the nonreciprocal hopping. That is, the distribution in one site will dominate the two-site localized state in the non-Hermitian case. As a result, the IPR_g increases with g for the higher-site localized states.

Moreover, one finds that IPR_g under OBC has a minimum between the plateaux and the transition region, as shown in the insert of Fig. 7(a). This indicates the appearance of the critical phase. For these critical modes, we find that the self-similar structure is still preserved under the PBC as shown in Fig. 9(a). In addition, for the OBC, the wave function is distributed in one side but not at the boundary, as shown in Fig. 9(b).

B. Excited states

Besides IPR_g , similar cascade structures can also be found in the excited states. In the AA model limit, the localization transition appears simultaneously at $\lambda_c = 2e^g$, as shown in Fig. 10(a). By continuously tuning β toward the Fibonacci

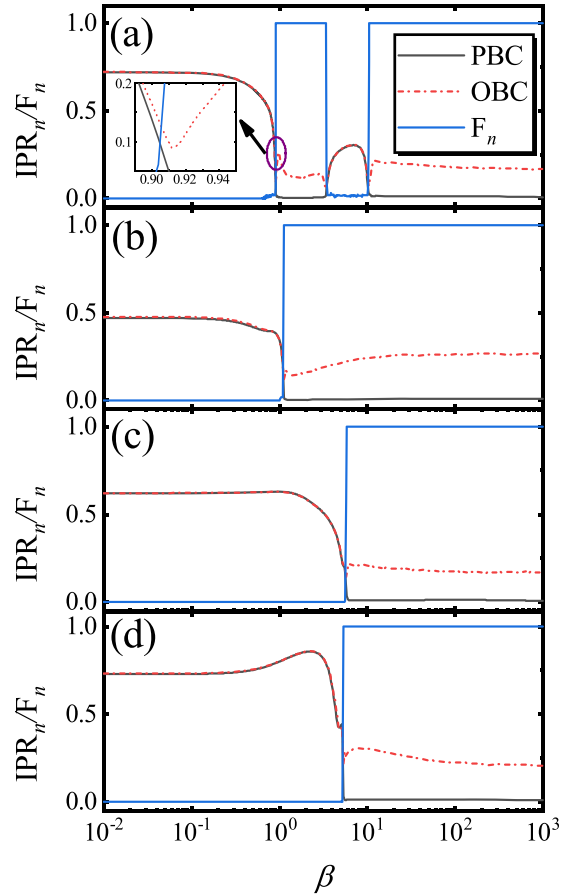


FIG. 11. IPR_n versus β under PBC and OBC and F_n versus β under PBC for n th excited states. Here we use $\lambda = 5$, $g = 0.5$, $L = 610$, and $n = 100, 200, 300, 500$ for (a), (b), (c), and (d), respectively. IPR_n and F_n are averaged for 500 choices of ϕ . The inset in (a) shows the minimum of IPR_n under OBC, indicating the critical point.

limit starting from the strongly localized AA model, we find that the lowest set of eigenstates becomes delocalized first at $\beta \sim 1$ and then return to be localized at $2 < \beta < 10$, as shown in Fig. 10(b). In addition, for the higher sets of excited eigenstates, the cascade behavior does not appear for the present range of β as shown in Fig. 10(b).

It has been found that the localization transition can be accompanied with the real-complex transition of the eigenenergies in some non-Hermitian systems [39,40]. For the non-Hermitian IAAF model (1), the ground state is real since the time-reversal symmetry is still preserved. However, for the excited states, we find that the real-complex transition and the localization transition occur at almost the same point. A function F_n , measuring the value of the imaginary part of the energy, is defined as

$$F_n = \begin{cases} 0, & \text{Im}(E_n) = 0, \\ 1, & \text{Im}(E_n) \neq 0. \end{cases} \quad (5)$$

In Fig. 11, curves of IPR_n versus β under PBC and OBC and F_n versus β under PBC for different excited states are plotted. One finds that the cascade of the delocalization transition is accompanied by the cascade of the real-complex transition.

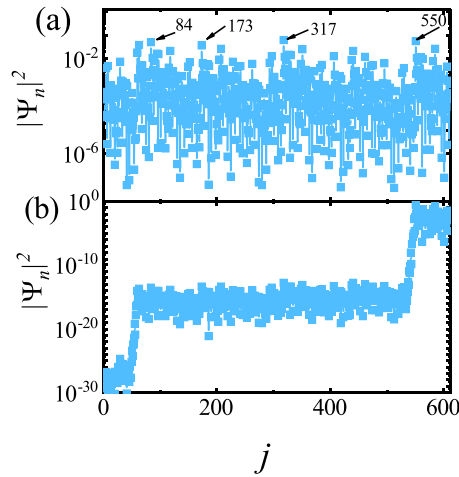


FIG. 12. Typical spatial distribution of critical mode for the excited state under PBC (a) and OBC (b). Here we use $\beta = 0.9311$, $L = 610$, $g = 0.5$, $\phi = 0$ and $\lambda = 5$. These parameters correspond to the critical point as shown in the inset in Fig. 11(a).

For the critical excited states, the spatial distribution also has the self-similar structure similar to that of the ground state. In Fig. 12, the spatial distribution of the critical mode of the excited state under PBC and OBC is also plotted. One finds that the relative distance between the peaks follows the Fibonacci sequence under the PBC. For the OBC, the spatial distribution localizes on one side but not at the boundary.

V. EXPERIMENT FEASIBILITY

Here we discuss possible experimental approaches to detect the cascade of the delocalization transition in the non-Hermitian IAAF model. On the one hand, the Hermitian IAAF model has been experimentally realized in a photonic platform [25]. By engineering the cavity-polariton samples, the cascade of delocalization transition has been examined therein. On the other hand, the experimental scheme of non-Hermiticity has been proposed, e.g., the ultracold atomic system [49], the RLC electronic circuit [34], and the photonic system [78]. In particular, the non-Hermiticity violating the left-right symmetry has been observed in a PT-symmetric optical system [79]. Based on these experimental progressions, we expect that the non-Hermitian IAAF could be realized in experiments. Our theoretical results could be tested therein.

VI. SUMMARY

In this paper, we have studied the cascade of the delocalization transition and the critical behavior in a non-Hermitian IAAF model. In the non-Hermitian AA limit, the system undergoes a delocalization transition at $\lambda_c = 2e^g$. At the critical point, the spatial distribution of ground state has a self-similar structure under the PBC. Under the OBC, the wave function of the critical mode in the non-Hermitian AA limit localizes in one side but not at the boundary, which is different from the non-Hermitian skin effect. By calculating the IPR_g , we find that the IPR_g of the critical mode in non-Hermitian AA limit scales as $\text{IPR}_g \propto L^\nu$ with $\nu = -0.1189$. This demon-

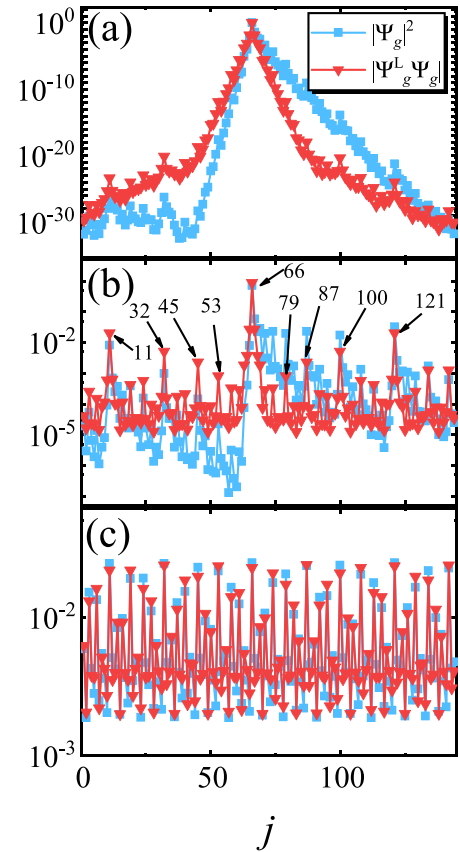


FIG. 13. Typical spatial distributions of $|\Psi_g^L \Psi_g|$ and $|\Psi_g|^2$ for (a) the localized phase of the non-Hermitian AA limit, (b) the critical phase of the non-Hermitian AA limit, and (c) the extended phase of the non-Hermitian AA limit. Here we use $L = 144$, $\phi = 1.3090$, $\beta = 10^{-10}$, $g = 0.5$ and $\lambda = 5$ in (a), $\lambda = 2e^g$ in (b), $\lambda = 2$ in (c).

strates that the non-Hermitian AA model and the Hermitian AA model belong to different universality classes. In the non-Hermitian Fibonacci limit, we find that the system is always in the extended phase for any finite g and λ , since IPR_g scales as $\text{IPR}_g \propto L^{-1}$. By tuning β continuously from the non-Hermitian AA limit into the non-Hermitian Fibonacci limit, the cascade of delocalization transition is found for both the ground and the excited states, but only a few plateaux appear. These results demonstrate that the nonreciprocal hopping can drastically change the cascade behavior in the IAAF model. In addition, we have shown that the spatial distributions of the critical state between two plateaux still have a self-similar structure. Moreover, we have found that the real-complex transition also demonstrates cascade behavior, similar to the delocalization transition for the excited states.

Besides the nonreciprocal hopping, the non-Hermiticity can also be induced by the on-site gain/loss [31,39,78,80,81]. It should be interesting to study the delocalization transition and the critical behavior in the IAAF model with on-site gain/loss. For example, the AA model with a complex phase $\phi = \theta + ih$ has been explored in Ref. [31], which shows that this model hosts a topological phase transition by tuning h . Thus it is intriguing to explore the topological properties in the cascade process of delocalization transition in the IAAF model with this AA model limit. This work is still in process.

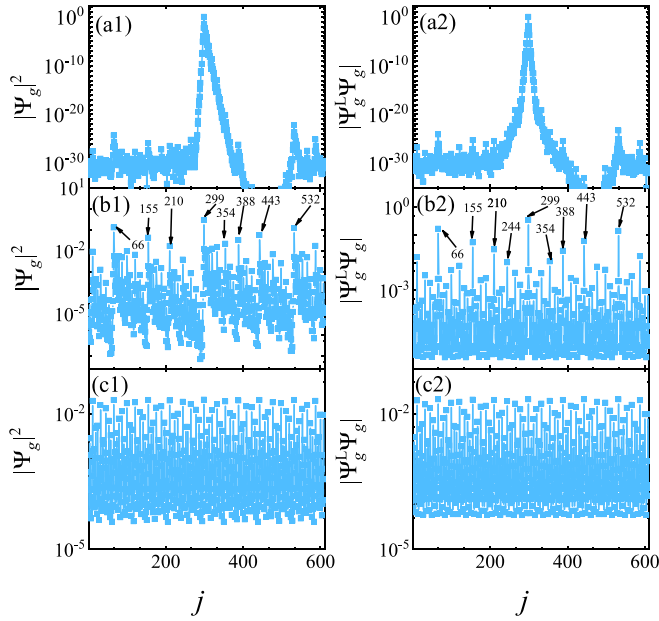


FIG. 14. Typical spatial distributions of $|\Psi_g^L \Psi_g|$ and $|\Psi_g|^2$ for [(a1) and (a2)] the localized phase, [(b1) and (b2)] the critical phase, and [(c1) and (c2)] the extended phase along the transition from the non-Hermitian AA limit to the non-Hermitian Fibonacci limit. Here we use $L = 610$, $\lambda = 5$, $g = 0.5$, $\phi = 1.3090$, and $\beta = 0.2$ in (a1) and (a2), $\beta = 0.85$ in (b1) and (b2), and $\beta = 1$ in (c1) and (c2).

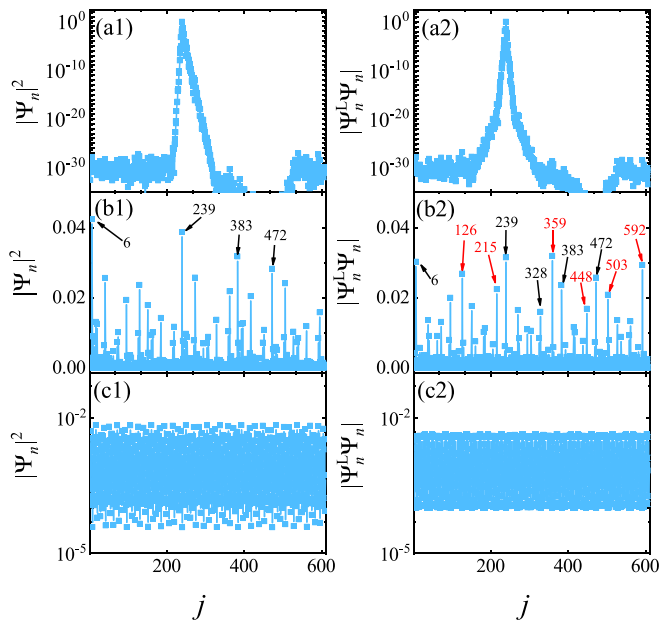


FIG. 15. Typical spatial distributions of $|\Psi_n|^2$ and $|\Psi_n^L \Psi_n|$ for [(a1) and (a2)] the localized phase, [(b1) and (b2)] the critical phase, and [(c1) and (c2)] the extended phase along the transition from the non-Hermitian AA limit to the non-Hermitian Fibonacci limit. Here we use $L = 610$, $\lambda = 5$, $g = 0.5$, $\phi = 1.3090$, $n = 100$, and $\beta = 0.2$ in (a1) and (a2), $\beta = 0.9311$ in (b1) and (b2), and $\beta = 2$ in (c1) and (c2). In (b2), the black and red labels correspond to two different Fibonacci sequences.

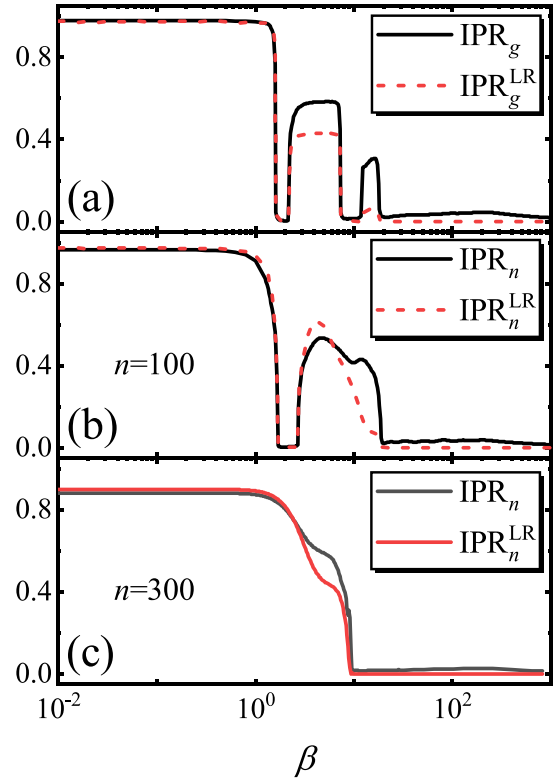


FIG. 16. IPR^{LR} and IPR as functions of β for (a) the ground state and [(b) and (c)] two n th excited states. Here we use $\lambda = 10$, $g = 0.5$, $L = 610$, and $n = 100$ and 300 for (b) and (c), respectively. IPR^{LR} and IPR are averaged over 500 choices of ϕ .

ACKNOWLEDGMENTS

L.-J.Z. is supported by the Natural Science Foundation of Jiangsu Province (Grant No. BK20170309), National Natural science Foundation of China (Grant No. 11704161) and China Postdoctoral Science Foundation (Grant No. 2021M691535). S.Y. is supported by the National Natural science Foundation of China (Grant No. 41030090) and the start-up funding in Sun Yat-Sen University (Grant No. 74130-18841290).

APPENDIX: DIAGNOSING THE DELOCALIZATION TRANSITION VIA MIXED WAVE FUNCTIONS

In Ref. [29], it was shown that the mixed production $|\Psi^L \Psi|$, in which $\Psi^L(g) = \Psi(-g)^\dagger$, can provide more appropriate information in diagnosing the delocalization phase and the delocalization transition in non-Hermitian disordered systems. In this Appendix, we show the behavior of $|\Psi^L \Psi|$ in model (1) and compare the results from $|\Psi|^2$.

In Fig. 13, we show the distribution of $|\Psi^L \Psi|$ in different phases of the ground state of model (1) in its AA limit and compare the distribution with $|\Psi|^2$. One finds that in different phases, $|\Psi^L \Psi|$ and $|\Psi|^2$ demonstrate similar characteristic behaviors, although the detailed information is

different. In the localized phase [Fig. 13(a)], both $|\Psi^L\Psi|$ and $|\Psi|^2$ develop peaks at the same position; in the delocalized phase [Fig. 13(c)], both $|\Psi^L\Psi|$ and $|\Psi|^2$ show uniform distributions; at the critical point [Fig. 13(b)], both $|\Psi^L\Psi|$ and $|\Psi|^2$ exhibit tips, whose distances obey the Fibonacci sequence.

In addition, Fig. 14 shows the results in the ground state of the IAAF model. As demonstrated in Fig. 6, the localization-delocalization transition can be tuned by β . We show in Fig. 14 that $|\Psi^L\Psi|$ and $|\Psi|^2$ show similar behaviors in different phases for different β . Moreover, Fig. 15 shows that similar behaviors also happen in the excited states, in which the energy spectra are complex. Interestingly, here, at the critical point, Fig. 15(b2) shows that the tips of $|\Psi^L\Psi|$ are arranged according to two interlaced Fibonacci sequences.

To further explore whether $|\Psi^L\Psi|$ can diagnose the cascade of delocalization transitions, we define a modified IPR,

which reads

$$\text{IPR}_n^{\text{LR}} = \frac{\sum_{j=1}^L |\Psi_n^L(j)\Psi_n(j)|^2}{\sum_{j=1}^L |\Psi_n^L(j)\Psi_n(j)|}. \quad (\text{A1})$$

Figure 16 shows IPR_n^{LR} in both the ground state and the two excited states. By comparing with the results of IPR, we find that both of them can characterize the cascade of delocalization transitions.

Our results seem at variance with those reported in Ref. [29], which reported that the delocalization phase for the complex spectra should be characterized by $|\Psi^L\Psi|$. A possible reason is that the present model is a model with quasiperiodic potential, rather than the random model studied in Ref. [29]. If so, our results, combined with Ref. [29], show that the disorder correlation can affect the indicator of the delocalization transition.

[1] S. Aubry and G. André, *Ann. Israel Phys. Soc.* **3**, 133 (1980).
 [2] S. Schiffer, X.-J. Liu, H. Hu, and J. Wang, *Phys. Rev. A* **103**, L011302 (2021).
 [3] Y. Lahini, R. Pugatch, F. Pozzi, M. Sorel, R. Morandotti, N. Davidson, and Y. Silberberg, *Phys. Rev. Lett.* **103**, 013901 (2009).
 [4] H. Hiramoto and M. Kohmoto, *Phys. Rev. Lett.* **62**, 2714 (1989).
 [5] S. Y. Jitomirskaya, *Ann. Math.* **150**, 1159 (1999).
 [6] N. Macé, A. Jagannathan, P. Kalugin, R. Mosseri, and F. Piéchon, *Phys. Rev. B* **96**, 045138 (2017).
 [7] H. Yao, H. Khoudli, L. Bresque, and L. Sanchez-Palencia, *Phys. Rev. Lett.* **123**, 070405 (2019).
 [8] U. Agrawal, S. Gopalakrishnan, and R. Vasseur, *Nat. Commun.* **11**, 2225 (2020).
 [9] D. R. Hofstadter, *Phys. Rev. B* **14**, 2239 (1976).
 [10] Y. E. Kraus, Y. Lahini, Z. Ringel, M. Verbin, and O. Zilberberg, *Phys. Rev. Lett.* **109**, 106402 (2012).
 [11] M. Verbin, O. Zilberberg, Y. E. Kraus, Y. Lahini, and Y. Silberberg, *Phys. Rev. Lett.* **110**, 076403 (2013).
 [12] S. Ganeshan, K. Sun, and S. Das Sarma, *Phys. Rev. Lett.* **110**, 180403 (2013).
 [13] V. Mastropietro, *Phys. Rev. Lett.* **115**, 180401 (2015).
 [14] S. Xu, X. Li, Y.-T. Hsu, B. Swingle, and S. Das Sarma, *Phys. Rev. Research* **1**, 032039(R) (2019).
 [15] A. Sinha, M. M. Rams, and J. Dziarmaga, *Phys. Rev. B* **99**, 094203 (2019).
 [16] Z. Xu and S. Chen, *Phys. Rev. A* **103**, 043325 (2021).
 [17] Q.-B. Zeng, Y.-B. Yang, and Y. Xu, *Phys. Rev. B* **101**, 020201(R) (2020).
 [18] Q.-B. Zeng and Y. Xu, *Phys. Rev. Research* **2**, 033052 (2020).
 [19] M. Kohmoto, L. P. Kadanoff, and C. Tang, *Phys. Rev. Lett.* **50**, 1870 (1983).
 [20] S. Ostlund, R. Pandit, D. Rand, H. J. Schellnhuber, and E. D. Siggia, *Phys. Rev. Lett.* **50**, 1873 (1983).
 [21] R. Merlin, K. Bajema, R. Clarke, F. Y. Juang, and P. K. Bhattacharya, *Phys. Rev. Lett.* **55**, 1768 (1985).
 [22] E. Maciá, *Phys. Rev. B* **60**, 10032 (1999).
 [23] J. A. Ashraff and R. B. Stinchcombe, *Phys. Rev. B* **40**, 2278 (1989).
 [24] F. Domínguez-Adame, *Physica B* **307**, 247 (2001).
 [25] V. Goblot, A. Štrkalj, N. Pernet, J. L. Lado, C. Dorow, A. Lemaître, L. Le Gratiet, A. Harouri, I. Sagnes, S. Ravets, A. Amo, J. Bloch, and O. Zilberberg, *Nat. Phys.* **16**, 832 (2020).
 [26] Y. E. Kraus and O. Zilberberg, *Phys. Rev. Lett.* **109**, 116404 (2012).
 [27] N. Hatano and D. R. Nelson, *Phys. Rev. Lett.* **77**, 570 (1996).
 [28] N. Hatano and D. R. Nelson, *Phys. Rev. B* **56**, 8651 (1997).
 [29] N. Hatano and D. R. Nelson, *Phys. Rev. B* **58**, 8384 (1998).
 [30] A. V. Kolesnikov and K. B. Efetov, *Phys. Rev. Lett.* **84**, 5600 (2000).
 [31] S. Longhi, *Phys. Rev. Lett.* **122**, 237601 (2019).
 [32] S. Longhi, *Phys. Rev. B* **100**, 125157 (2019).
 [33] X. Cai, *Phys. Rev. B* **103**, 014201 (2021).
 [34] H. Jiang, L.-J. Lang, C. Yang, S.-L. Zhu, and S. Chen, *Phys. Rev. B* **100**, 054301 (2019).
 [35] Y. Liu, Y. Wang, X.-J. Liu, Q. Zhou, and S. Chen, *Phys. Rev. B* **103**, 014203 (2021).
 [36] A. Jazaeri and I. I. Satija, *Phys. Rev. E* **63**, 036222 (2001).
 [37] J. Feinberg and A. Zee, *Phys. Rev. E* **59**, 6433 (1999).
 [38] P. Wang, L. Jin, and Z. Song, *Phys. Rev. A* **99**, 062112 (2019).
 [39] R. Hamazaki, K. Kawabata, and M. Ueda, *Phys. Rev. Lett.* **123**, 090603 (2019).
 [40] L.-J. Zhai, S. Yin, and G.-Y. Huang, *Phys. Rev. B* **102**, 064206 (2020).
 [41] L.-Z. Tang, G.-Q. Zhang, L.-F. Zhang, and D.-W. Zhang, *Phys. Rev. A* **103**, 033325 (2021).
 [42] T. Liu, H. Guo, Y. Pu, and S. Longhi, *Phys. Rev. B* **102**, 024205 (2020).
 [43] X. Cai, *arXiv:2103.04107* (2021).

- [44] Y. Huang and B. I. Shklovskii, *Phys. Rev. B* **101**, 014204 (2020).
- [45] Y. Huang and B. I. Shklovskii, *Phys. Rev. B* **102**, 064212 (2020).
- [46] M.-L. Yang, H. Wang, C.-X. Guo, X.-R. Wang, G. Sun, and S.-P. Kou, [arXiv:2006.10278](https://arxiv.org/abs/2006.10278) (2020).
- [47] Y. Xu, S.-T. Wang, and L. M. Duan, *Phys. Rev. Lett.* **118**, 045701 (2017).
- [48] F. K. Kunst, E. Edvardsson, J. C. Budich, and E. J. Bergholtz, *Phys. Rev. Lett.* **121**, 026808 (2018).
- [49] Z. Gong, Y. Ashida, K. Kawabata, K. Takasan, S. Higashikawa, and M. Ueda, *Phys. Rev. X* **8**, 031079 (2018).
- [50] S. Yao, F. Song, and Z. Wang, *Phys. Rev. Lett.* **121**, 136802 (2018).
- [51] L.-J. Zhai and S. Yin, *Phys. Rev. B* **102**, 054303 (2020).
- [52] S. Yao and Z. Wang, *Phys. Rev. Lett.* **121**, 086803 (2018).
- [53] F. Song, S. Yao, and Z. Wang, *Phys. Rev. Lett.* **123**, 170401 (2019).
- [54] N. Okuma, K. Kawabata, K. Shiozaki, and M. Sato, *Phys. Rev. Lett.* **124**, 086801 (2020).
- [55] K. Kawabata, M. Sato, and K. Shiozaki, *Phys. Rev. B* **102**, 205118 (2020).
- [56] D. S. Borgnia, A. J. Kruchkov, and R.-J. Slager, *Phys. Rev. Lett.* **124**, 056802 (2020).
- [57] S. Longhi, *Phys. Rev. B* **102**, 201103(R) (2020).
- [58] Y. Fu, J. Hu, and S. Wan, *Phys. Rev. B* **103**, 045420 (2021).
- [59] J. S. Liu, Y. Z. Han, and C. S. Liu, *Chin. Phys. B* **29**, 010302 (2020).
- [60] V. M. Martinez Alvarez, J. E. Barrios Vargas, and L. E. F. Foa Torres, *Phys. Rev. B* **97**, 121401(R) (2018).
- [61] K. Zhang, Z. Yang, and C. Fang, *Phys. Rev. Lett.* **125**, 126402 (2020).
- [62] Z. Yang, K. Zhang, C. Fang, and J. Hu, *Phys. Rev. Lett.* **125**, 226402 (2020).
- [63] Y. Yi and Z. Yang, *Phys. Rev. Lett.* **125**, 186802 (2020).
- [64] T. Yoshida, T. Mizoguchi, and Y. Hatsugai, *Phys. Rev. Research* **2**, 022062(R) (2020).
- [65] T. Yoshida, R. Peters, and N. Kawakami, *Phys. Rev. B* **98**, 035141 (2018).
- [66] K. Kawabata, T. Bessho, and M. Sato, *Phys. Rev. Lett.* **123**, 066405 (2019).
- [67] S. Yin, G.-Y. Huang, C.-Y. Lo, and P. Chen, *Phys. Rev. Lett.* **118**, 065701 (2017).
- [68] B. Dora, M. Heyl, and R. Moessner, *Nat. Commun.* **10**, 2254 (2019).
- [69] K. Ding, G. Ma, M. Xiao, Z. Q. Zhang, and C. T. Chan, *Phys. Rev. X* **6**, 021007 (2016).
- [70] L. Li, C. H. Lee, S. Mu, and J. Gong, *Nat. Commun.* **11**, 5491 (2020).
- [71] L.-J. Zhai, H.-Y. Wang, and S. Yin, *Phys. Rev. B* **97**, 134108 (2018).
- [72] C. M. Bender and S. Boettcher, *Phys. Rev. Lett.* **80**, 5243 (1998).
- [73] C. M. Bender, *Rep. Prog. Phys.* **70**, 947 (2007).
- [74] F. Evers and A. D. Mirlin, *Phys. Rev. Lett.* **84**, 3690 (2000).
- [75] E. Cuevas, *Phys. Rev. B* **66**, 233103 (2002).
- [76] K. Kawabata and S. Ryu, *Phys. Rev. Lett.* **126**, 166801 (2021).
- [77] R. Hamazaki, K. Kawabata, N. Kura, and M. Ueda, *Phys. Rev. Research* **2**, 023286 (2020).
- [78] B. Midya, H. Zhao, and L. Feng, *Nat. Commun.* **9**, 2674 (2018).
- [79] C. E. Rüter, K. G. Makris, R. El-Ganainy, D. N. Christodoulides, M. Segev, and D. Kip, *Nat. Phys.* **6**, 192 (2010).
- [80] D. Leykam, S. Flach, and Y. D. Chong, *Phys. Rev. B* **96**, 064305 (2017).
- [81] D. V. Novitsky, D. Lyakhov, D. Michels, D. Redka, A. A. Pavlov, and A. S. Shalin, *Sci. Rep.* **11**, 4790 (2021).